

# Enhanced Readout and Sensitivity of Diamond N-V Centers Coupled to Hyperbolic Metamaterial Photonic Cavities

Jonathan Bar-David,<sup>1,2,3,\*</sup> Sigal A. Wolf,<sup>2,3,4</sup> S. R. K. Chaitanya Indukuri,<sup>1,2,3</sup> Rotem Malkinson,<sup>1,2,3</sup>  
Noa Mazurski,<sup>1,2,3</sup> Uriel Levy,<sup>1,2,3</sup> and Nir Bar-Gill<sup>1,2,3,4,†</sup>

<sup>1</sup>Applied Physics Department, The Hebrew University of Jerusalem, Jerusalem, 9190401, Israel

<sup>2</sup>The Center of Nano-Science and Nanotechnology, The Hebrew University of Jerusalem, Jerusalem, 9190401, Israel

<sup>3</sup>The Quantum Center, The Hebrew University of Jerusalem, Jerusalem, 9190401, Israel

<sup>4</sup>Racach Institute of Physics, The Hebrew University of Jerusalem, Jerusalem, 9190401, Israel

(Received 14 November 2022; revised 6 February 2023; accepted 1 May 2023; published 27 June 2023)

Nitrogen-vacancy (N-V) centers are diamond lattice defects that may be manipulated and controlled by visible light and microwave irradiation. They are considered a promising solid-state platform for a broad range of quantum technologies, such as magnetic field sensing. A major limitation in realizing such applications is the weak optical signal attained from the NVs, making the readout inefficient and prone to noise. Here, we report the increased brightness and shortened lifetime of N-V centers coupled to hyperbolic metamaterial photonic cavities with optimized dispersion characteristics. As a result, we demonstrate the enhancement of magnetic field sensitivity and measurement SNR. These results introduce a broadly applicable, robust, and technically accessible platform, promising improved performance relevant for a multitude of solid-state defects and their applications.

DOI: 10.1103/PhysRevApplied.19.064074

## I. INTRODUCTION

Negatively charged nitrogen-vacancy (N-V) centers in diamond are structural defects that have well-defined energy states within the diamond band gap [1–7]. N-V centers are among the solid-state systems with the longest spin-coherence time at room temperature and at low temperatures [8]. The spin states and energy levels of electrons bound to N-V centers are easily manipulated by interactions with microwaves (MWs) at a few gigahertz and by light in the visible and short-wavelength-infrared (SWIR) regimes [2,9–11], and therefore this physical system is considered a potential candidate for quantum technologies such as quantum sensing (particularly, magnetic field sensing), quantum communications, and quantum simulation and computing [12–16].

Despite these novel properties (i.e., easy manipulation and long coherence times), the phonon broadened emission of the N-V and the high refractive index of diamond severely limit their interaction with radiation, and thus make them a faint source with inefficient optical readout of their spin or energy state [11,17,18].

In recent years, numerous researchers have attempted to address this issue and enhance the N-V centers'

emission rate (i.e., assist in radiating photons) by coupling the N-V centers to photonic structures [11,17,19–23]. The effect of the photonic structures may be understood in two complementary ways [24,25]: Quantum mechanically, a photonic structure (such as a cavity) increases the density of photonic states in the near field of the N-V center, thus increasing the probability of radiative decay [17,24–27]. Classically, the photonic structure may act as an antenna, providing impedance matching between the small N-V dipole and outgoing (or impinging) radiation [24,25]. As commented by Bogdanov *et al.* [11], this approach usually uses either dielectric structures as high- $Q$  cavities, which “trap” light in the region of N-V centers to increase interaction time and the local density of states, or metallic structures, which basically act as antennas for light [28,29], providing strong field enhancement and impedance matching, but also introducing losses.

In this manuscript, we report the use of hyperbolic metamaterial (HMM) cavities to enhance the emission of diamond N-V centers. HMM cavities are highly dispersive metal-dielectric nanoscale hybrid structures, made of alternating ultrathin films of metals and dielectric materials. The alternating layers create an effective highly anisotropic material with hyperbolic dispersion—namely, it reacts to radiation either as a metal or as a dielectric material, depending on the polarization [30–38]. Owing to this

\*jonathan.bardavid@mail.huji.ac.il

†bargill@phys.huji.ac.il

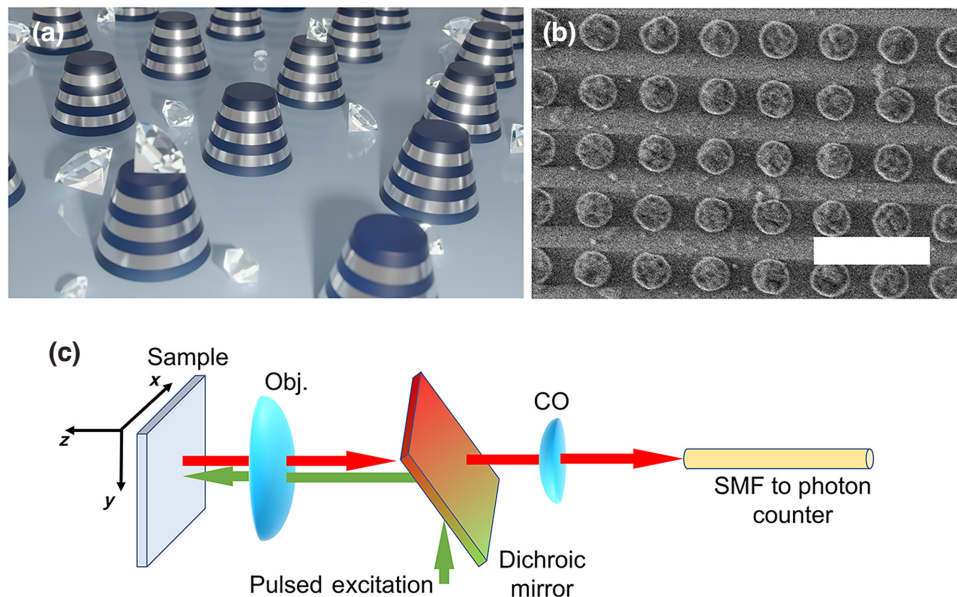


FIG. 1. (a) Artist's view of our samples, with ordered arrays of HMM cavities made of interleaved metallic and dielectric layers. Nanodiamonds are randomly placed between HMM cavities. (b) SEM of our fabricated HMM arrays. Diamonds are not seen due to the poor contrast between them and the substrate. Scale bar is 500 nm. (c) Schematics of the optical system used for the presented measurements. Sample is mounted on a three-axis piezo stage. Obj., main objective,  $60\times$ , NA = 0.95; CO, coupling optics (a set of lenses and a  $20\times$  objective); SMF, single-mode fiber leading to a single-photon counting module.

curious behavior, nanocavities made of HMMs support optical modes with ultrahigh  $K$ -vectors [24,25], which has proved particularly useful for interacting with nanoemitters or small dipoles [24,25].

As we show in this report, the coupling of HMM cavities to N-V centers in nanodiamonds (NDs) yields an enhancement of the emitted radiation, shortening of N-V lifetime, and increased signal-to-noise ratio (SNR) in magnetic field measurements [23]. This platform thus paves the way for a robust performance boost relevant for a broad range of solid-state defect systems and their corresponding quantum technology applications.

## II. RESULTS

### A. HMM cavity characterization

Our HMM cavities, an example of which is depicted in Fig. 1(b), are designed to have strong scattering resonances in the range of 600–800 nm. Owing to fabrication imperfections, the actual radius is slightly smaller than designed, and the cavities experience a slight inhomogeneous broadening in their dimensions. As a result, the sharp resonance seen in the simulation [Fig. 2(a)] is less distinct and at shorter wavelengths than planned; the measured result is presented in Fig. 2(b). It is worth noting

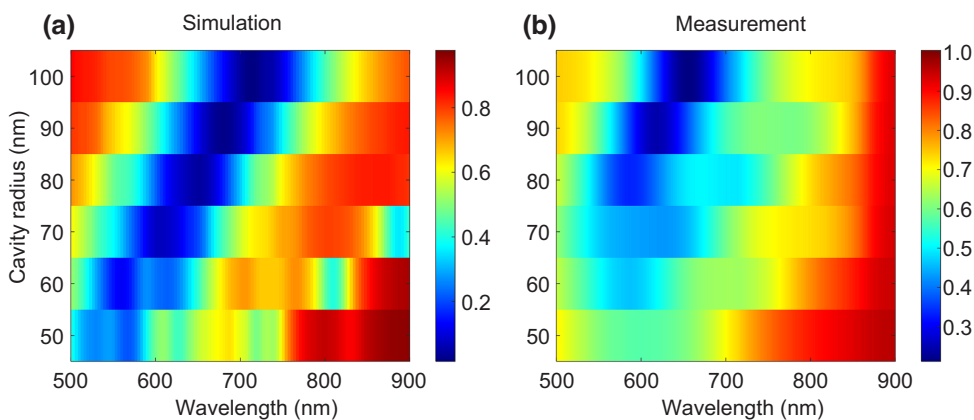


FIG. 2. Transmission spectra for HMM cavity arrays. (a) Simulation. (b) Measurement. The minima in the transmission spectra are the insignia of scattering resonances, coupling radiation to the structures' eigenmodes. It may be seen that the measured spectrum is slightly shifted from the calculated spectrum, due to nominal fabricated radii being slightly smaller than designed.

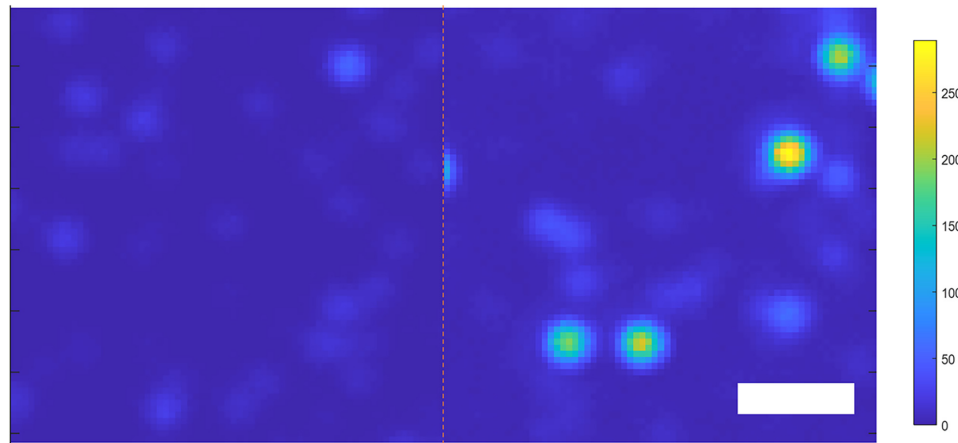


FIG. 3. Two confocal raster scans, each of  $7 \times 7 \mu\text{m}^2$  with 100-nm steps. Left side, NDs on bare glass; right side, NDs on HMM cavity array with  $R = 100 \text{ nm}$  and filling fraction = 20%. Scale bar length is  $2 \mu\text{m}$ . The emission of NDs on the HMM cavity array is considerably stronger. Colorbar units: kCounts per second.

that these scattering resonances are high-order modes of the individual HMM cavities as reported before [24,25], and are not grating-type resonances, which depend upon intercavity distances and produce surface waves.

### B. Emission enhancement

To characterize the emission of the NDs we use the home-built confocal microscopy setup sketched in Fig. 1(c). A pulsed green (532 nm) excitation laser is directed through a dichroic mirror into an objective lens, the excitation is focused upon the sample, and the emitted fluorescence is collected by the same objective. The red fluorescent light passes through the dichroic mirror and then the coupling optics, a set of lenses and a  $20\times$

objective, which direct the radiation into a single-mode fiber (SMF), connected at its other end to a single-photon counting module (SPCM).

Figure 3 shows side-by-side and on the same scale two confocal raster scans of NDs on bare glass (left-hand side) and on an HMM cavity array with a cavity radius of 100 nm and a filling fraction of 20% (i.e., a center-to-center distance of approximately 396 nm). The difference in ND brightness is apparent, specifically for the four ultrabright diamonds with intensities above  $1.5 \times 10^5$  counts/s. Qualitatively, a similar difference can also be observed for the other NDs.

In Fig. 4 and Table I we quantify these differences through statistics on five different types of structures: (i) NDs on bare glass; (ii) on “bulk” HMM, i.e., a region on

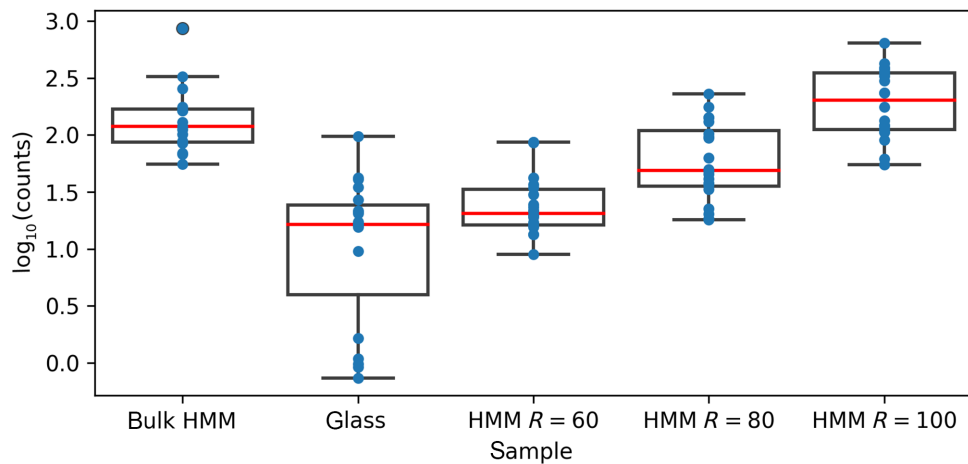


FIG. 4. Statistical data on the emission of nanodiamonds on different structures. The emissions of NDs placed on HMM cavity arrays are significantly stronger than those on bare glass substrate. Black box shows the middle 50% of data, black whiskers show 1.5 times the interquartile range (i.e., nearly 97% of population), red line marks the median. HMM cavity radius given in nanometers.

TABLE I. Distribution of nanodiamond intensities on different structures: summary of the data presented in Fig. 2. All values (except for observations) are given in kcps.

Photonic structure	Mean	SD	Min	Max	Range	Median	Observations
Bulk HMM	185.15	202.91	55.20	868.43	813.22	119.30	15
Glass	21.15	22.49	0.73	97.25	96.52	16.45	19
HMM $R = 60$	30.35	24.09	8.96	86.80	77.84	20.50	22
HMM $R = 80$	77.50	59.94	17.99	229.84	211.85	49.05	20
HMM $R = 100$	236.45	155.77	54.95	642.68	587.73	205.15	20

unpatterned interleaved layers [24]; and (iii) on arrays of HMM cavities with cavity radii of 60, 80, and 100 nm, with a constant filling fraction (FF) of 20% (the filling fraction is defined as the portion of the array area covered by metal, i.e.,  $FF = \pi R^2 / D^2$  where  $R$  is the cavity radius and  $D$  is the array periodicity). All structures are fabricated on the same glass substrate and are measured in the same setup under identical experimental conditions without moving the substrate.

Our results show an increase in ND brightness (as shown in thousands of counts per second) with increasing HMM cavity size. This is in accord with our transmission measurements shown in Fig. 2, identifying a strong optical resonance for HMM cavities with a radius of 100 nm around a wavelength of 650 nm, immediately above the N-V centers' zero-phonon line (ZPL,  $\lambda_{ZPL} = 637$  nm). Interestingly, the enhancement seems to affect not only the brightest diamonds, but also the faintest diamonds, and this is seen to be stronger for those on HMM compared with those on glass. Overall, we see more than an order of magnitude increase in the brightness for NDs that are coupled to our HMM cavities. The average distance between a ND and the closest cavity should be of the order of 2 times the cavity radius (a filling fraction of 20% implies an array periodicity of around 4 times cavity radius), and therefore we would expect an average enhancement of 5–10 times, which is indeed in good agreement with our observation. This enhancement is a result of the high-order modes of the HMM cavities. These modes support ultrahigh wave vectors, which provide the impedance matching for excited N-V dipoles to outcoupled radiation. See Supplemental Material [39] for the enhancement calculation, which is also addressed in Ref. [24].

It is worthwhile noting that the large variation in brightness levels of NDs on bulk HMM is attributed to one ultrabright outlier, while the majority of measured NDs are brighter than NDs on glass but dimmer than those on the 100-nm cavities. This result, along with the ND characteristic size (40 nm), leads us to believe that the NDs are located primarily between the cavities and probably not on top of them—NDs on top of the cavities should have very high enhancement, which would manifest as a well-distinguished group with narrow distribution in the data presented in Fig. 4.

### C. Lifetime shortening

The effect of enhancing the photonic density of states, as discussed previously, would be an increased probability for photon emission and a shortening of the excited-state lifetime. This is a manifestation of the Purcell effect, which describes enhanced emission rates by coupling to the electromagnetic modes. [17,24–26,40]. To identify such a process, we perform lifetime measurements on our samples by illuminating them with a pulsed green laser at 532 nm with a pulse width of 40 ps, and collecting time-resolved fluorescence.

Figure 5 shows normalized data of the excited state lifetime in five diamonds, each on one of our five different structures (i.e., glass, bulk HMM, and three types of HMM cavity array), and each being the median lifetime measurement for its sample. It is evident from the plots that the NDs coupled to HMM cavities have a significantly shorter lifetime. Together with the enhanced brightness reported previously, this draws a picture of true enhancement of radiative processes from NDs coupled to HMM cavities, establishing the main result of this paper. It should be noted that lifetime shortening alone does not guarantee

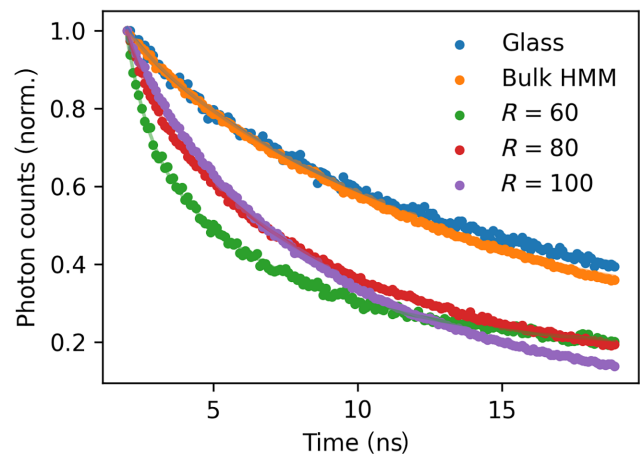


FIG. 5. Lifetime shortening in HMM cavity arrays. For each type of structure (bare glass, bulk HMM, and three types of HMM cavity array), the lifetime of the median diamond is plotted. HMM cavities show a significant decrease in the emission lifetime compared with NDs on bare glass. Fitted curves for each dataset are plotted by a continuous line.

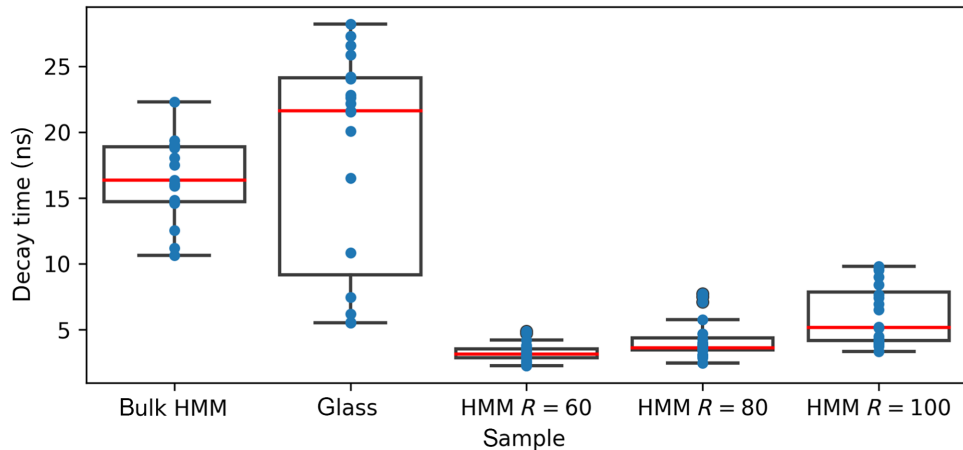


FIG. 6. Lifetimes of nanodiamonds coupled to different photonic structures. NDs coupled to HMM cavities decay significantly faster than NDs on glass. HMM cavity radius given in nanometers.

enhanced radiation due to the possibility of photons being absorbed by the structure (quenching) or emitted into the structure's dark (nonradiative) modes, while increased brightness without lifetime shortening may be a result of better coupling of the excitation light.

In Fig. 6 and Table II we detail the quantitative analysis of lifetime data from all structures. The data are fitted by exponential decays convoluted with our system's instrument response function (IRF). NDs on glass and bulk (unpatterned) HMM are fitted by two exponential functions, while those coupled to HMM cavity arrays are fitted by three exponents—the superfast decay of AgS in the cavities [41] (see Supplemental Material [39] for details of the AgS PL and decay IRF); the decay to the HMM-cavity mode; and the decay directly from the ND to radiation. The results clearly indicate that the lifetime of NDs coupled to HMM cavities is shortened, while the shortening itself seems to be dependent on the exact properties of the structure. Comparing lifetimes of NDs coupled to HMM cavities with a designed radius of 100 nm to NDs on glass shows an average decrease in measured lifetime of 3 to 5 times, which is equivalent to a Purcell factor of the same magnitude. It is worth noting that for HMM cavities with a radius of 60 nm we observe a significant lifetime shortening but no increase in brightness (presented in Fig. 3 above). While not thoroughly investigated, this is likely due to coupling of the NDs to dark cavity modes in the

structure [38,42–45]. This is in contrast to the cavities with a radius of 100 nm, which enhance the emission of light to the far field. From the lifetime measurement, the quality factor of our cavities can be estimated as  $Q \approx 5$ . Previous calculations [24] indicate that the mode volume in these cavities may be as small as  $5 \times 10^{-5} \lambda^3$ . The modest decrease in excited-state lifetime is attributed to the fact that the N-V centers are quite far from the field maximum [26]. This is another indication for NDs being around the cavities, where the electromagnetic fields are decaying rapidly with distance [24]. Additionally, the enhancement depends on dipole orientation, with the strongest enhancement affecting vertically oriented dipoles (which are the weakest when placed on glass). See Supplemental Material [39] for a numerical analysis of this enhancement. Finally, while the lifetime of NDs on bulk HMM is slightly shorter (compared with glass) the emission is nearly ten-fold stronger, as presented in Fig. 4. We attribute this behavior (enhanced emission without shortening lifetime) to the increase in collection efficiency by the bulk HMM as reported in Ref. [21].

#### D. ODMR contrast, SNR, and magnetic field sensitivity

An often-discussed application of N-V centers is magnetometry, particularly high-spatial resolution

TABLE II. Distribution of nanodiamonds' lifetimes on different structures: summary of the data presented in Fig. 6. All values (except observations) are given in nanoseconds.

Photonic structure	Avg.	SD	Min	Max	Range	Median	Observations
Bulk HMM	16.40	3.15	10.63	22.32	11.69	16.33	12
Glass	18.13	8.17	5.48	28.22	22.74	21.64	19
HMM R = 60	3.25	0.68	2.22	4.85	2.63	3.11	22
HMM R = 80	4.23	1.51	2.43	7.71	5.28	3.61	19
HMM R = 100	6.06	2.23	3.30	9.79	6.50	5.14	18

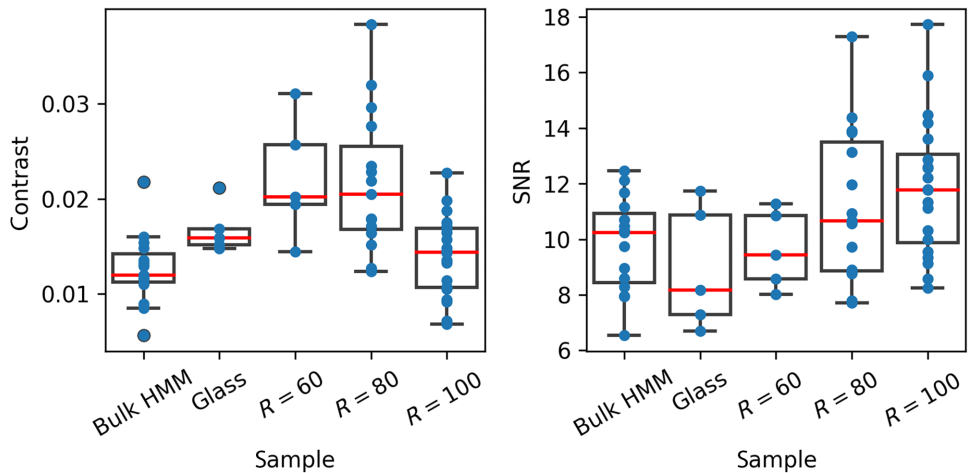


FIG. 7. ODMR contrast (left) and SNR (right) for nanodiamonds coupled to different structures. Left-hand side, NDs coupled to HMM cavities with large radii show an unexplained decrease in ODMR contrast. Right-hand side, despite lower contrast, actual SNR for NDs coupled to HMMs is superior due to the higher brightness. Showing all data points with average count rate greater than  $10^4$  counts/s. HMM cavity radius given in nanometers.

magnetometry, allowed by the small size and volume of N-V centers. Often, dc magnetometry would be carried out by performing optically detected magnetic resonance (ODMR) spectroscopy on a precharacterized sample; changes to the magnetic field in the environment of the N-V center would be identified as a change in the spectral response.

The sensitivity of such a measurement is characterized by [10]

$$\eta = P_F \left( \frac{h}{g\mu_B} \right) \frac{\Delta\nu\sigma\sqrt{t_m}}{\alpha\beta},$$

given in units of  $G/\sqrt{\text{Hz}}$ .  $\eta$  is the smallest recognizable change in the magnetic field for a given experimental system and measurement (averaging) time. This expression is composed of natural constants:  $h/g\mu_B = 1/\gamma$ , where  $h$  is Planck's constant,  $g$  is the electron  $g$ -factor,  $\mu_B$  is Bohr's magneton, and  $\gamma$  is the gyromagnetic ratio for the electrons in the N-V center,  $\gamma \cong 2.8 \text{ MHz/G}$ ;  $P_F$  is a constant accounting for the spectral line shape;  $\Delta\nu$  is the ODMR resonance width in hertz;  $\alpha$  is the ODMR contrast (i.e., a unitless number; in our system it is typically around 0.02);  $\beta$  is the number of collected photons (depending on the specific diamond and photonic cavity; in our

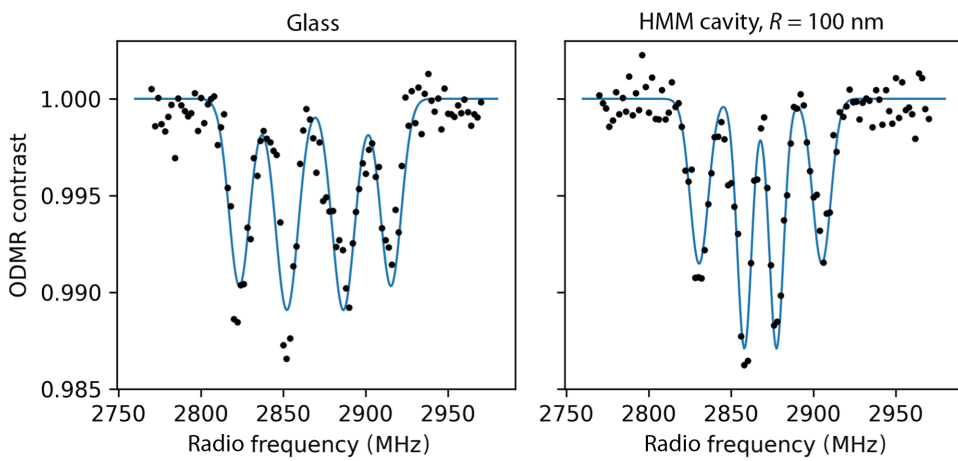


FIG. 8. ODMR measurement of two specific NDs. Left, ND on glass substrate; right, ND on HMM cavity array, with cavity radius 100 nm. Fitted curves assume two symmetric Gaussian-shaped resonances, with axis of symmetry taken as a fitting parameter near 2870 MHz. These are taken while applying a constant magnetic field of about 15 G. The multiple resonances of each ND are associated with the multiple N-V centers inside each ND, which appear at different orientations, and thus are differently affected by the magnetic field and the coupling to the HMM structure. The fitted curves determine the diamond on HMM structure has a narrower linewidth (6.1 vs. 8.9 MHz), and a higher contrast compared with the diamond on glass, which leads to an improved sensitivity for magnetic fields.

TABLE III. Magnetic field sensitivity of different nanodiamonds on photonic structures showing the increased magnetic field sensitivity of nanodiamonds coupled to HMM arrays. The sensitivity is evaluated from curve-fitting results, the details of which are in the Supplemental Material [39].

Photonic structure	Diamond no.	Center frequency (MHz)	Fitted contrast (a.u.)	Resonance width $\Delta\nu$ (MHz)	SNR (a.u.)	Count rate (kcps)	$\Delta\nu/\text{SNR}$ (Hz)
Glass	6	2722	0.012	8.3	8.2	18.9	1.016
Glass	9	2761	0.011	7.2	8.0	0.5	0.902
HMM $R = 60$ nm	6	2731	0.01	5.6	8.6	14.3	0.653
HMM $R = 60$ nm	14	2788	0.01	3.9	9.4	33.8	0.414
HMM $R = 80$ nm	1	2721	0.012	10.1	13.1	51.2	0.769
HMM $R = 100$ nm	4	2809	0.01	3.5	15.9	122.8	0.220

system it varies between 1 and 400);  $\sigma$  is the measurement noise (standard deviation); and  $t_m$  is the measurement time (which is held constant for all our measurements). One can also define the signal of this measurement as  $\alpha\beta$ , such that the sensitivity is given by

$$\eta = P_F \left( \frac{h}{g\mu_B} \right) \frac{\Delta\nu}{\text{SNR}} \sqrt{t_m},$$

where  $\text{SNR} = \sigma/\alpha\beta$ . For the case of shot-noise-limited measurements, the noise is  $\sigma = \sqrt{\beta}$ , and the sensitivity becomes  $\eta = P_F(h/g\mu_B)(\Delta\nu t_m/\alpha\sqrt{\beta})$ .

In this work, we perform ODMR measurements on a single specific system (and, moreover, on the same glass substrate), comparing NDs on glass with those on various nanocavity structures. Thus, our comparison in terms of magnetic measurement (ODMR) and sensitivity are fair (of course, in the average sense), with the significant change between measured NDs resulting from their location with respect to the photonic structures. In Fig. 7 we plot statistical data for the contrast and SNR of ODMR resonances on different photonic structures. Despite weak changes in contrast induced by the HMM cavity structures, the overall SNR of our measurement increases, mostly due to the increase in the N-V brightness (see Supplemental Material [39] for details of SNR for all measurements).

Based on the presented calculation, tying N-V brightness to SNR and magnetic field sensitivity, we measure the magnetic field sensitivities of specific NDs on our samples. To that end, we analyze the ODMR spectra of these samples (Fig. 8), fitting the resonance features and extracting the relevant parameters (including resonance width, contrast, and noise).

We use  $\Delta\nu/\text{SNR}$  as the figure of merit for magnetic field sensitivity, calculate it for each of our ODMR results, and compare this value with different measurements across the different photonic structures.

We select resonances with contrasts of roughly 1%–1.2% to compare magnetic field sensitivity. Our results are presented in Table III.

The photonic structures increase ODMR sensitivity (as manifested by our figure of merit  $\Delta\nu/\text{SNR}$ ) by 1.5 times on average, while the sensitivity increase of specific diamonds can be up to 5 times depending on the exact spectral line shape (see Supplemental Material [39] for curve fitting of ODMR spectra). The SNR statistics shown in Fig. 7 (and in the Supplemental Material) present a broad picture regarding the possibility of enhanced readout and superior sensitivity from N-V centers coupled to photonic structures.

### III. DISCUSSION AND CONCLUSIONS

In this report we establish the enhanced brightness and shortened lifetimes of N-V centers in NDs coupled to HMM cavities. We also indicate the significance of this enhancement to magnetic field measurements, resulting in higher sensitivity and better SNR, which are both desirable in all proposed N-V applications related to quantum sensing and quantum technologies. The robustness and technical simplicity of the presented structures, the availability and ease of dispersion of NDs, along with the enhanced performance measured, suggest that the approach described here could have broad implications in nearly every N-V-based experiment and technological application, such as high spatial resolution or *in vitro* magnetometry [46–48].

As no “special” features of NDs have been exploited in this research, we do not expect these results to change considerably if these experiments are to be repeated with N-V centers in bulk diamond; however, the lifetime distribution may be narrower in bulk and annealed crystals.

We note that in this work we invest significant effort in collecting sufficient data on multiple ND samples. Our data suggest that N-V properties such as lifetime, brightness, and ODMR contrast have a large variability; therefore, statistics of multiple measurements are essential in discussing NDs, and possibly other types of nanoemitters such as quantum dots. For example, the average lifetime of NDs on glass presented in Fig. 6 and Table II is around 18 ns, with a standard deviation as high as around 8.4 ns.

This variation, likely arising from the specific properties of each ND (such as N-V-center number, orientation, clustering, surface defects, etc.) cannot be overlooked.

The variability of ND brightness raises an additional question regarding the true concentration of NDs on our surfaces; our data suggest that the ND concentration is larger on HMM cavity arrays than on glass. It is unclear whether this is due to the mechanical effect of the different surfaces, or due to emission enhancement of faint diamonds, which becomes detectable with coupling to HMM cavities. Finally, while our measurements do not indicate a clear correlation between the coupling of NDs to HMM photonic structures and ODMR contrast, it has been recently suggested that HMM cavities may couple external dc magnetic fields with light [49], potentially causing changes to ND magnetic behavior. This is not addressed within the scope of this report and will be studied in future work.

## IV. EXPERIMENTAL TECHNIQUES

### A. HMM fabrication

HMMs are fabricated by electron-beam (*e*-beam) lithography on glass substrates using the following protocol:

Glass substrates are cleaned and spin-coated by a 280-nm layer of PMMA 495 A5 used as *e*-beam resist. Immediately before *e*-beam exposure, the samples are coated by a thin film of *E*-spacer 300z (Resonac Inc.) to avoid charging during the *e*-beam writing process. Substrates are exposed by a 100-keV beam in an *e*-beam lithography tool (Elionix Inc.). Following exposure, the *E*-spacer layer is dissolved in water and the patterns developed in a mixture of Methyl isobutyl ketone and isopropyl alcohol with a volume-volume ratio of 1:3 (MIBK/IPA 1:3). The HMM layers (Ag, Al<sub>2</sub>O<sub>3</sub>) are deposited by *e*-beam evaporation (VST evaporator); and finally, the structures are created by lifting off the resist in hot acetone. As a final step, the entire sample is coated by a 5-nm film of Al<sub>2</sub>O<sub>3</sub> as a protective layer.

### B. Optical characterization of HMMs

HMM samples are characterized by home-built optical transmission measurements in the visible and SWIR: the structures are illuminated with the light from a tungsten-halogen lamp; transmitted light is collected by a Nikon-Eclipse TE inverted microscope with a 50× objective and directed into a multimode fiber connected to a spectrometer (Ocean Optics, Flame). The measurements are referenced by the spectrum measured on the glass substrate. Each measurement is averaged 100 times.

Photoluminescence of HMM structures is measured by a confocal Raman microscope (InVia, Renishaw) [41, 50], exciting the sample by illumination at 515 nm, and

detecting luminescence up to 750 nm through a dedicated spectrometer.

### C. Photonics simulations

Photonic structures are simulated by finite difference time domain (FDTD) software (Lumerical Inc., FDTD engine). Details are given in recent publications [24, 51], and see Supplemental Material [39] for full simulation details.

### D. Deposition of nanodiamonds

We use NDs with a high density of N-V centers, with a characteristic size of 40 nm, and suspended in deionized water (Adamas Nanotechnologies, Inc.). The suspended NDs are stirred in an ultrasonic bath for 20 min to dissolve aggregates, and then mixed with DI water with 0.15% of polyvinyl alcohol (weight/weight); ND concentration in DI water is 20 µg/ml (weight/volume), resulting in a surface density of around 0.3 ND/µm<sup>2</sup> on glass. Except for the single ultrabright ND on bulk HMM, we see no evidence for aggregates in our measurements—they do not appear in SEMs, and do not seem to appear in our optical measurements. We expect aggregates to be brighter but have lower ODMR contrast than single NDs; however, the ODMR measurements we perform are on NDs with brightness over 10<sup>4</sup> counts/s, and no correlation (or anticorrelation) between brightness and ODMR contrast is found.

### E. Diamond characterization

Characterization of NDs is performed on a home-built reflection-mode confocal microscope. The NDs are excited by a pulsed 532-nm laser with average power of about 600 µW (in our system this value is within the N-V saturation regime). The fluorescence is filtered by two dichroic mirrors and two additional band-pass filters, achieving a filtration ratio of around 10<sup>-10</sup> (with a cut-on wavelength at 650 nm), which is checked to be sufficient for stopping the reflection of the excitation beam. The fluorescence is coupled to single-mode fibers leading to SPCMs (Excelitas Technologies). The signal from these detectors is monitored by a time-tagger unit (Swabian Instruments), with a timing resolution of 30 ps. Continuous-wave ODMR measurements are controlled by a pulse streamer (Swabian Instruments). All electronics are computer controlled.

The sample is mounted on three-axis motorized stages (Physik Instrumente) allowing for two-dimensional raster scanning of the sample.

All samples are fabricated on a single glass slide so measurements of different structures require only shifting of the stage and no sample remounting to assure identical measurement conditions.

For electron spin resonance ODMR measurements, a thin copper wire is held above the sample providing sufficient power for such experiments, driven by a signal

generator (SRS), and amplified by a solid-state amplifier (ZHL-25W-63+). A dc magnetic field of around 50 G is applied by a permanent magnet held about 2 cm above the sample (K&J Magnetics). The ODMR contrast is typically around 2%; this is attributed mainly to the large distance ( $>1$  mm) between rf source and NDs. Reports of ND ODMR contrast vary between about 2% and 15%, depending on system geometry and ND type [22,52–54].

### F. Data collection

To collect data from multiple NDs the sample is raster scanned over regions of  $5 \times 5$  to  $10 \times 10 \mu\text{m}^2$  with steps of 100 nm; NDs are detected by image recognition tools; then each diamond is targeted to measure its lifetime and its ODMR spectrum. The number of tested NDs in each experiment is usually between 20 and 30 diamonds.

### G. Data analysis

Data analysis on single diamonds (including the evaluation of brightness, lifetime, ODMR contrast, etc.) is performed automatically by MATLAB scripts. Statistical analysis on large datasets (finding medians, means, etc.) is performed by variability plots using JMP software and plotted using PYTHON.

All data is available from the corresponding author upon reasonable request.

### ACKNOWLEDGMENT

The authors thank Dr. Christian Frydendahl for his beautiful graphics.

- [1] F. Jelezko, T. Gaebel, I. Popa, M. Domhan, A. Gruber, and J. Wrachtrup, Observation of Coherent Oscillation of a Single Nuclear Spin and Realization of a Two-Qubit Conditional Quantum Gate, *Phys. Rev. Lett.* **93**, 130501 (2004).
- [2] M. W. Doherty, N. B. Manson, P. Delaney, F. Jelezko, J. Wrachtrup, and L. C. L. Hollenberg, The nitrogen-vacancy colour centre in diamond, *Phys. Rep.* **528**, 1 (2013).
- [3] E. Bourgeois, A. Jarmola, P. Siyushev, M. Gulka, J. Hraby, F. Jelezko, D. Budker, and M. Nesladek, Photoelectric detection of electron spin resonance of nitrogen-vacancy centres in diamond, *Nat. Commun.* **6**, 1 (2015).
- [4] A. Lenef and S. C. Rand, Electronic structure of the N-V center in diamond: Theory, *Phys. Rev. B* **53**, 13441 (1996).
- [5] G. Davies, Charge states of the vacancy in diamond, *Nature* **269**, 498 (1977).
- [6] J. A. Larsson and P. Delaney, Electronic structure of the nitrogen-vacancy center in diamond from first-principles theory, *Phys. Rev. B* **77**, 165201 (2008).
- [7] V. M. Acosta, A. Jarmola, E. Bauch, and D. Budker, Optical properties of the nitrogen-vacancy singlet levels in diamond, *Phys. Rev. B* **82**, 201202 (2010).
- [8] N. Bar-Gill, L. M. Pham, A. Jarmola, D. Budker, and R. L. Walsworth, Solid-state electronic spin coherence time approaching one second, *Nat. Commun.* **4**, 1 (2013).
- [9] I. Lovchinsky, J. D. Sanchez-Yamagishi, E. K. Urbach, S. Choi, S. Fang, T. I. Andersen, K. Watanabe, T. Taniguchi, A. Bylinskii, E. Kaxiras, *et al.*, Magnetic resonance spectroscopy of an atomically thin material using a single-spin qubit, *Science* **355**, 503 (2017).
- [10] L. M. Pham, *Magnetic Field Sensing with Nitrogen Vacancy Color Centers in Diamond* (Harverad, Cambridge, Massachusetts, 2013).
- [11] S. I. Bogdanov, M. Y. Shalaginov, A. S. Lagutchev, C.-C. Chiang, D. Shah, A. S. Baburin, I. A. Ryzhikov, I. A. Rodionov, A. V. Kildishev, A. Boltasseva, *et al.*, Ultrabright room-temperature sub-nanosecond emission from single nitrogen-vacancy centers coupled to nanopatch antennas, *Nano Lett.* **18**, 4837 (2018).
- [12] L. Robledo, L. Childress, H. Bernien, B. Hensen, P. F. A. Alkemade, and R. Hanson, High-fidelity projective readout of a solid-state spin quantum register, *Nature* **477**, 574 (2011).
- [13] B. J. Shields, Q. P. Unterreithmeier, N. P. de Leon, H. Park, and M. D. Lukin, Efficient Readout of a Single Spin State in Diamond via Spin-to-Charge Conversion, *Phys. Rev. Lett.* **114**, 136402 (2015).
- [14] J. R. Maze, P. L. Stanwix, J. S. Hodges, S. Hong, J. M. Taylor, P. Cappellaro, L. Jiang, M. V. G. Dutt, E. Togan, A. S. Zibrov, *et al.*, Nanoscale magnetic sensing with an individual electronic spin in diamond, *Nature* **455**, 644 (2008).
- [15] A. Morello, J. J. Pla, F. A. Zwanenburg, K. W. Chan, K. Y. Tan, H. Huebl, M. Möttönen, C. D. Nugroho, C. Yang, J. A. van Donkelaar, *et al.*, Single-shot readout of an electron spin in silicon, *Nature* **467**, 687 (2010).
- [16] D. A. Hopper, R. R. Grote, A. L. Exarhos, and L. C. Bassett, Near-infrared-assisted charge control and spin readout of the nitrogen-vacancy center in diamond, *Phys. Rev. B* **94**, 241201 (2016).
- [17] S. A. Wolf, I. Rosenberg, R. Rapaport, and N. Bar-Gill, Purcell-enhanced optical spin readout of nitrogen-vacancy centers in diamond, *Phys. Rev. B* **92**, 235410 (2015).
- [18] M. Steiner, P. Neumann, J. Beck, F. Jelezko, and J. Wrachtrup, Universal enhancement of the optical readout fidelity of single electron spins at nitrogen-vacancy centers in diamond, *Phys. Rev. B* **81**, 035205 (2010).
- [19] N. H. Wan, S. Mouradian, and D. Englund, Two-dimensional photonic crystal slab nanocavities on bulk single-crystal diamond, *Appl. Phys. Lett.* **112**, 141102 (2018).
- [20] S. Mouradian, N. H. Wan, T. Schröder, and D. Englund, Rectangular photonic crystal nanobeam cavities in bulk diamond, *Appl. Phys. Lett.* **111**, 21103 (2017).
- [21] M. Y. Shalaginov, V. V. Vorobyov, J. Liu, M. Ferrera, A. V. Akimov, A. Lagutchev, A. N. Smolyaninov, V. V. Klimov, J. Irudayraj, A. V. Kildishev, *et al.*, Enhancement of single-photon emission from nitrogen-vacancy centers with TiN/(Al, Sc)N hyperbolic metamaterial, *Laser Photonics Rev.* **9**, 120 (2015).
- [22] H. Guo, Y. Chen, D. Wu, R. Zhao, J. Tang, Z. Ma, C. Xue, W. Zhang, and J. Liu, Plasmon-enhanced sensitivity of spin-based sensors based on a diamond ensemble of nitrogen vacancy color centers, *Opt. Lett.* **42**, 403 (2017).

- [23] S. Bogdanov, M. Y. Shalaginov, A. Akimov, A. S. Lagutchev, P. Kapitanova, J. Liu, D. Woods, M. Ferrera, P. Belov, J. Irudayaraj, *et al.*, Electron spin contrast of Purcell-enhanced nitrogen-vacancy ensembles in nanodiamonds, *Phys. Rev. B* **96**, 035146 (2017).
- [24] S. R. K. C. Indukuri, J. Bar-David, N. Mazurski, and U. Levy, Ultrasmall mode volume hyperbolic nanocavities for enhanced light-matter interaction at the nanoscale, *ACS Nano* **13**, 11770 (2019).
- [25] S. R. K. Chaitanya Indukuri, C. Frydendahl, J. Bar-David, N. Mazurski, and U. Levy, WS<sub>2</sub> Monolayers coupled to hyperbolic metamaterial nanoantennas: Broad implications for light-matter-interaction applications, *ACS Appl. Nano Mater.* **3**, 10226 (2020).
- [26] E. M. Purcell, Spontaneous Emission Probabilities at Radio Frequencies, *Phys. Rev.* **69**, 674 (1946).
- [27] S. Haroche and D. Kleppner, Cavity quantum electrodynamics, *Phys. Today* **42**, 24 (1989).
- [28] L. Novotny and N. van Hulst, Antennas for light, *Nat. Photonics* **5**, 83 (2011).
- [29] A. I. Kuznetsov, A. E. Miroshnichenko, M. L. Brongersma, Y. S. Kivshar, and B. Luk'yanchuk, Optically resonant dielectric nanostructures, *Science* **354**, aag2472 (2016).
- [30] S. R. K. Chaitanya Indukuri, J. Bar-David, N. Mazurski, and U. Levy, in *Optics InfoBase Conference Papers*, (2019) Vol. Part F128.
- [31] J. Yao, X. Yang, X. Yin, G. Bartal, and X. Zhang, Three-dimensional nanometer-scale optical cavities of indefinite medium, *Proc. Natl. Acad. Sci. U. S. A.* **108**, 11327 (2011).
- [32] L. Li, W. Wang, T. S. Luk, X. Yang, and J. Gao, Enhanced quantum dot spontaneous emission with multilayer metamaterial nanostructures, *ACS Photonics* **4**, 501 (2017).
- [33] A. V. Kildishev, A. Boltasseva, and V. M. Shalaev, Planar photonics with metasurfaces, *Science* **339**, 1232009 (2013).
- [34] C. Indukuri, R. K. Yadav, and J. K. Basu, Broadband room temperature strong coupling between quantum dots and metamaterials, *Nanoscale* **9**, 11418 (2017).
- [35] K.-T. Tsai, G. A. Wurtz, J.-Y. Chu, T.-Y. Cheng, H.-H. Wang, A. V. Krasavin, J.-H. He, B. M. Wells, V. A. Podolskiy, J.-K. Wang, *et al.*, Looking into meta-atoms of plasmonic nanowire metamaterial, *Nano Lett.* **11**, 4971 (2014).
- [36] Z. Jacob, J. Y. Kim, G. V. Naik, A. Boltasseva, E. E. Narimanov, and V. M. Shalaev, Engineering photonic density of states using metamaterials, *Appl. Phys. B: Lasers Opt.* **100**, 215 (2010).
- [37] A. Poddubny, I. Iorsh, P. Belov, and Y. Kivshar, Hyperbolic metamaterials, *Nat. Photonics* **7**, 948 (2013).
- [38] T. Isoniemi, N. Maccaferri, Q. M. Ramasse, G. Strangi, and F. De Angelis, Electron energy loss spectroscopy of bright and dark modes in hyperbolic metamaterial nanostructures, *Adv. Opt. Mater.* **8**, 2000277 (2020).
- [39] See Supplemental Material at <http://link.aps.org/supplemental/10.1103/PhysRevApplied.19.064074> for further details of experiments and simulations.
- [40] C. Indukuri, A. Mukherjee, and J. K. Basu, Tailoring local density of optical states to control emission intensity and anisotropy of quantum dots in hybrid photonic-plasmonic templates, *Appl. Phys. Lett.* **106**, 131111 (2015).
- [41] D. Brühwiler, C. Leiggeler, S. Glaus, and G. Calzaferri, Luminescent silver sulfide clusters, *J. Phys. Chem. B* **106**, 3770 (2002).
- [42] S. Campione, S. Liu, L. I. Basilio, L. K. Warne, W. L. Langston, T. S. Luk, J. R. Wendt, J. L. Reno, G. A. Keeler, I. Brener, *et al.*, Broken symmetry dielectric resonators for high quality factor Fano metasurfaces, *ACS Photonics* **3**, 2362 (2016).
- [43] M. Liu, T.-W. Lee, S. K. Gray, P. Guyot-Sionnest, and M. Pelton, Excitation of Dark Plasmons in Metal Nanoparticles by a Localized Emitter, *Phys. Rev. Lett.* **102**, 107401 (2009).
- [44] A. Roberts, T. J. Davis, and D. E. Gomez, Dark mode metasurfaces: Sensing optical phase difference with subradiant modes and Fano resonances, *JOSA B* **34**, D95 (2017).
- [45] D. E. Gómez, Z. Q. Teo, M. Altissimo, T. J. Davis, S. Earl, and A. Roberts, The dark side of plasmonics, *Nano Lett.* **13**, 3722 (2013).
- [46] H. C. Davis, P. Ramesh, A. Bhatnagar, A. Lee-Gosselin, J. F. Barry, D. R. Glenn, R. L. Walsworth, and M. G. Shapiro, Mapping the microscale origins of magnetic resonance image contrast with subcellular diamond magnetometry, *Nat. Commun.* **9**, 1 (2018).
- [47] L. T. Hall, G. C. G. Beart, E. A. Thomas, D. A. Simpson, L. P. McGuinness, J. H. Cole, J. H. Manton, R. E. Scholten, F. Jelezko, J. Wrachtrup, *et al.*, High spatial and temporal resolution wide-field imaging of neuron activity using quantum N-V-diamond, *Sci. Rep.* **2**, 1 (2012).
- [48] Q. C. Sun, T. Song, E. Anderson, A. Brunner, J. Förster, T. Shalomayeva, T. Taniguchi, K. Watanabe, J. Gräfe, R. Stöhr, *et al.*, Magnetic domains and domain wall pinning in atomically thin CrBr<sub>3</sub> revealed by nanoscale imaging, *Nat. Commun.* **12**, 1 (2021).
- [49] J. Kuttruff, A. Gabbari, G. Petrucci, Y. Zhao, M. Iarossi, E. Pedrueza-Villalmanzo, A. Dmitriev, A. Paraccino, G. Strangi, F. De Angelis, *et al.*, Magnetic Circular Dichroism in Hyperbolic Metamaterial Nanoparticles, (2021).
- [50] L. X. Chen, D. W. Li, L. L. Qu, Y. T. Li, and Y. T. Long, SERS sensing of sulfide based on the sulfidation of silver nanoparticles, *Anal. Methods* **5**, 6579 (2013).
- [51] A. M. Morsy and M. L. Povinelli, Coupled metamaterial optical resonators for infrared emissivity spectrum modulation, *Opt. Express* **29**, 5840 (2021).
- [52] S. Sotoma, D. Terada, T. F. Segawa, R. Igarashi, Y. Harada, and M. Shirakawa, Enrichment of ODMR-active nitrogen-vacancy centres in five-nanometre-sized detonation-synthesized nanodiamonds: Nanoprobes for temperature, angle and position, *Sci. Rep.* **8**, 1 (2018).
- [53] Y. Nishimura, K. Oshimi, Y. Umehara, Y. Kumon, K. Miyaji, H. Yukawa, Y. Shikano, T. Matsubara, M. Fujiiwara, Y. Baba, *et al.*, Wide-field fluorescent nanodiamond spin measurements toward real-time large-area intracellular thermometry, *Sci. Rep.* **11**, 1 (2021).
- [54] Z. Al-Baiaty, B. P. Cumming, X. Gan, and M. Gu, Detection of the ODMR signal of a nitrogen vacancy centre in nanodiamond in propagating surface plasmons, *J. Opt.* **20**, 035001 (2018).